Functional Bimorph Composite Nanotapes

Rongrui He,[†] Matthew Law,[†] Rong Fan, Franklin Kim, and Peidong Yang*

Department of Chemistry, Materials Science Division, Lawrence Berkeley National Laboratory, University of California, Berkeley, California 94720

ABSTRACT

Single-crystalline nanoribbons were used as substrates for the epitaxial growth of different functional thin films deposited by laser ablation techniques. This simple method yields highly crystalline bilayer nanotapes with sharp structural and compositional interfaces. As an example, $Co_{0.05}Ti_{0.95}O_2@SnO_2$ nanotapes are shown to be ferromagnetic at room temperature. These composite nanotapes, with their various possible functionalities, represent an important new class of nanoscale building blocks for optoelectronic applications.

Nanowires with different cross-sectional shapes have attracted significant research interest due to their technological potential as unique types of nanoscale building blocks for future optoelectronic devices and systems.[1−3] Major efforts have been placed on methodology development for nanowire synthesis, assembly, and property elucidation. However, the bulk of previous studies is limited to simple binary semiconductors, with only a few recent investigations into complex systems such as superlattice nanowires[4−6] and ternary compounds.[7,8] A significant bottleneck in the field is the lack of a general approach to the synthesis of nanowire building blocks composed of complex functional materials (e.g., ternary and quaternary systems). Here we report a versatile approach to the synthesis of composite nanowire structures where the compositional limitation is no longer an issue and the resulting nanostructures could readily have multiple functionalities such as luminescence, ferromagnetism, ferroelectric, or superconducting properties. In this process, tin dioxide nanoribbons are used as substrates for thin-film growth using pulsed laser deposition (PLD). Various oxides (e.g., TiO_2, transition metal doped TiO_2, and ZnO) have been deposited on these one-dimensional nanoscale substrates. Electron microscopy and X-ray diffraction studies clearly demonstrate that these functional oxides grow epitaxially on the side surfaces of the substrate nanoribbons with sharp structural and compositional interfaces, and so form a unique class of bilayer nanoribbons (Figure 1a) with significantly enhanced functionality. As an example, the $Co_{0.05}Ti_{0.95}O_2@SnO_2$ nanotapes are shown to be ferromagnetic at room temperature.

The rutile SnO_2 nanoribbons used in this study were synthesized according to previously reported procedures.[9]

This synthetic method yields high aspect ratio (i.e., 100−2000) single-crystalline nanoribbons with $\langle 101 \rangle$ growth directions and well-faceted, nearly rectangular cross-sections bounded by $\{10\bar{1}\}$ and $\{010\}$ surface planes (Figures 1b,c).[9] The crystalline perfection and atomically flat surface facets of these nanoribbons make them excellent substrates for the epitaxial growth of materials with appropriate crystal symmetries. The good thermal stability of these oxide nanoribbons is equally important to their versatility as substrates because they can survive the harsh conditions required for many conceivable vapor deposition processes.

Pulsed laser ablation was used to deposit TiO_2, $Co_{0.05}Ti_{0.95}O_2$, or $BaTiO_3$ onto a collection of SnO_2 nanoribbons to yield composite nanotapes (Figure 1a). The ablation was carried out in oxygen atmospheres of 100−500 mTorr with the temperature, laser ablation parameters, and deposition time adjusted for each individual system. Figures 1b,d show typical field emission scanning electron microscope (FESEM) images of SnO_2 nanoribbons before and after TiO_2 coating. The pure SnO_2 nanoribbons have a smooth morphology with nearly rectangular cross-sectional dimensions averaging 30×120 nm (Figure 1c). The wide and narrow sides of a given nanoribbon adopt either the $\{010\}$ or $\{10\bar{1}\}$ planes. Figure 2a shows a transmission electron microscopy (TEM) image of two such nanoribbons with different wide side planes. Figures 2b,c are the TEM and high-resolution TEM (HRTEM) images of a nanoribbon with a (010) wide surface and a $(10\bar{1})$ narrow surface, while Figures 2d,e show the corresponding images for a nanoribbon with a $(10\bar{1})$ wide surface and a (010) narrow surface. Lattice spacing of 2.7 and 4.8 Å between the $(10\bar{1})$ and (010) planes can be clearly resolved in Figures 2c,e. The corresponding electron diffractions (insets in Figures 2c,e) further confirm these structural assignments.

* Corresponding author. E-mail: p_yang@uclink.berkeley.edu.
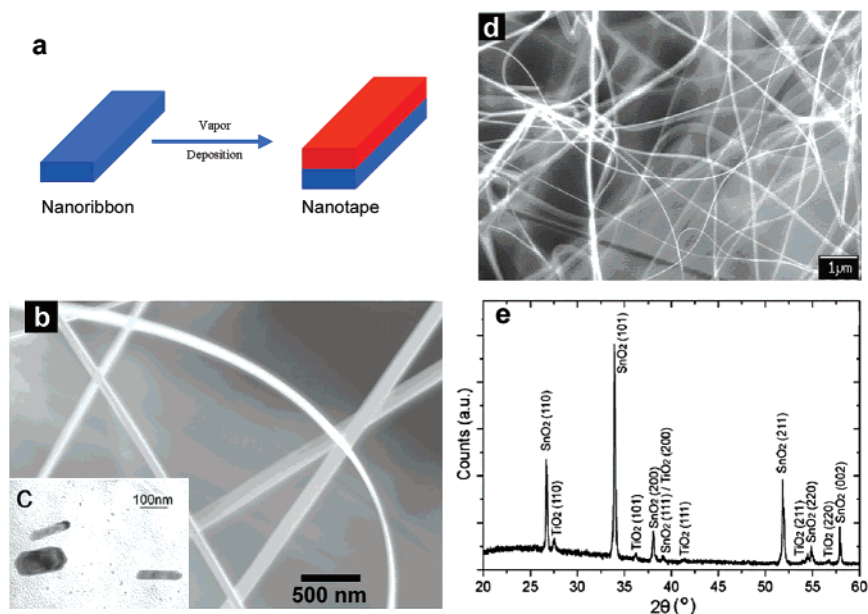† These authors contributed equally to this work.

Figure 1. (a) Schematic illustration of the use of nanoribbons as substrates to generate composite nanotape structures by pulsed laser deposition. (b, d) Scanning electron microscopy images of the SnO_2 nanoribbons (b) before and (d) after TiO_2 deposition using PLD. (c) Cross-sectional TEM image of the as-made nanoribbon. SnO_2 nanoribbons were synthesized using a simple thermal deposition process.[9] To synthesize nanotapes, a collection of SnO_2 nanoribbons was placed inside a quartz tube in a horizontal tube furnace near a sintered TiO_2 target, which was then ablated at 600 °C in 500 mTorr of flowing O_2 for 2−8 min by a frequency-doubled Nd:YAG laser (Spectra Physics) operating at 20−50 mJ/pulse and 3−10 Hz. It was found that usually only one side plane of a given nanoribbon was coated, and that the outermost ribbons in the collection intercepted most of the assorted material in the laser plume, thus allowing many of the inner ribbons to be coated uniformly. Image (d) is of a group of these inner nanoribbons. (e) An X-ray diffraction pattern of the $TiO_2@SnO_2$ composite nanotapes. The diffraction peaks are indexed according to the rutile SnO_2 and TiO_2 crystal structures.

The overall ribbon morphology is maintained after the deposition, and the average nanoribbon thickness increases (Figure 1d). X-ray diffraction taken on the resulting nanotapes (Figure 1e) shows two sets of diffraction peaks corresponding to the rutile SnO_2 and TiO_2 structures, with no other phases present.

Structural and compositional analysis was carried out on these samples to characterize the $TiO_2@SnO_2$ interface. Figure 3a shows a TEM image of a single composite nanotape, revealing its clean and sharp laminated morphology. It was found that the thin film coating on the nanoribbon is essentially single crystalline. The epitaxial nature of the interface was further characterized by HRTEM in detail. The TiO_2 deposition results in an atomically sharp interface between TiO_2 and SnO_2, as shown in Figure 3b. This particular nanotape has the TiO_2 epitaxially oriented on the narrow side (010) surface. The different lattice spacings for the two (010) planes of the rutile TiO_2 and SnO_2 structures (4.64 Å vs 4.84 Å) can be well resolved in Figure 3b. The electron diffractions taken on the two sides of the interface (insets in Figure 3b) further demonstrate that an excellent epitaxial relationship is established between the TiO_2 and SnO_2. In addition, Figure 3c presents a line profile of the elemental composition perpendicular to the tape axis, which also confirms the formation of an anisotropic bilayer nanotape structure with a smooth interface and external surface.

Importantly, a cross-sectional TEM image taken on a nanotape (Figure 3d) unambiguously reveals the quasi-rectangular bilayer morphology of the nanotape. Electron diffraction at the interface again shows only two sets of well-
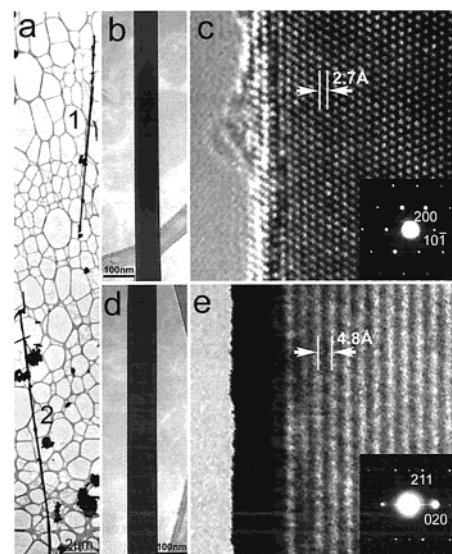

Figure 2. (a) TEM image of two as-made SnO_2 nanoribbons. (b−c) Low magnification and high-resolution TEM images of the nanoribbon indexed as "1" in (a). This ribbon has (010) as its wide side plane and (10$\bar{1}$) as its narrow side plane. 2.7 Å is the lattice spacing between the (10$\bar{1}$) planes. Inset shows an electron diffraction taken along the [010] zone axis. (d−e) Low magnification and high-resolution TEM images of the nanoribbon indexed as "2" in (a). This ribbon has (10$\bar{1}$) as its wide side plane and (010) as its narrow side plane. 4.8 Å is the lattice spacing between the (010) planes. Inset shows an electron diffraction taken along the [$\bar{1}$02] zone axis. The data were recorded on a Philip CM 200 transmission electron microscope operated at 200 keV.

correlated diffraction patterns that indicate the excellent interfacial epitaxial relationship between the two materials
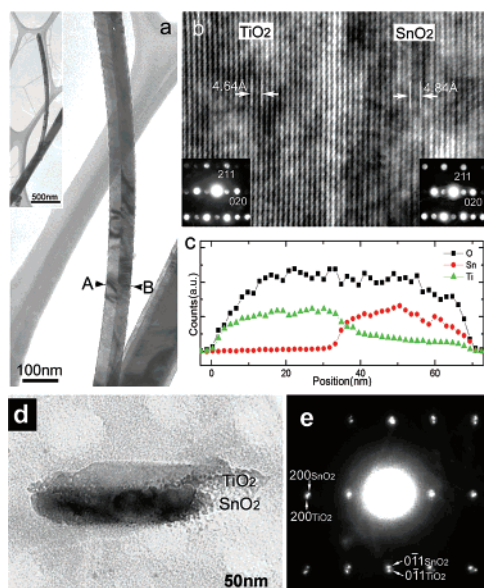
Figure 3. (a) TEM image of a TiO_2@SnO_2 nanotape; inset is its low magnification image. (b) HRTEM image of the atomically sharp TiO_2@SnO_2 interface. 4.64 and 4.84 Å correspond to the lattice spacing between the (010) planes in TiO_2 and SnO_2 rutile structures. Insets are electron diffractions taken on the two sides of the interface along the same [$\bar{1}$02] zone axes. (c) Compositional line profile across the TiO_2@SnO_2 interface as outlined in (a) (from A to B). (e) Selected area electron diffraction pattern recorded at the cross section area in (d). The SnO_2 and TiO_2 layers are in the same zone axis and have the same orientation, indicating perfect epitaxy.

(Figure 3e), except for this particular nanotape, the TiO_2 is epitaxially grown on the wide side (0$\bar{1}$1) plane. The energetic nature of the laser ablation process makes the plume highly directional and enables the selective film deposition on one side of the nanoribbon substrate due to the shadow effect. The epitaxy observed in these TiO_2@SnO_2 nanotapes is reasonable considering the relatively small lattice mismatch (2.9% for *a* and 7.0% for *c*) between the TiO_2 and SnO_2 rutile structures. Interfacial stress, however, does exist in these bimorph structures as seen in the TEM studies.

The same PLD approach was used to deposit Co-doped TiO_2 thin-films[10−13] on the SnO_2 nanoribbons in an effort to synthesize ferromagnetic semiconducting nanotapes. Figure 4 shows a series of TEM images of one such $Co_{0.05}$-$Ti_{0.95}O_2$@SnO_2 structure. The highly crystalline nature of the entire ~5 μm long nanotape, with its abrupt interface, smooth and uniform coating, can be readily seen here. Similarly, transition metal doped ZnO (e.g., $Mn_{0.1}Zn_{0.9}O$, $Ni_{0.1}Zn_{0.9}O$) has been successfully deposited on ZnO nanowires/ribbons to form homo-junctioned ZnO nanotapes. Importantly, we clearly observed ferromagnetic ordering at room temperature for the Co-doped rutile composite tape samples. Figure 5 shows magnetization (M) data as a function of the applied field (H) for a $Co_{0.05}Ti_{0.95}O_2$@SnO_2 nanotape sample. It must be emphasized that the formation of other phases $CoTiO_3$, $CoTi_2O_5$, Co, and CoO has not been observed in any of our electron microscopy and X-ray diffraction studies, probably due to the nature of nanoscale epitaxial growth in our process. This implies that the origin of the room temperature ferromagnetism in these composite nanotapes is intrinsically related to the Co-doped TiO_2.[10−13]
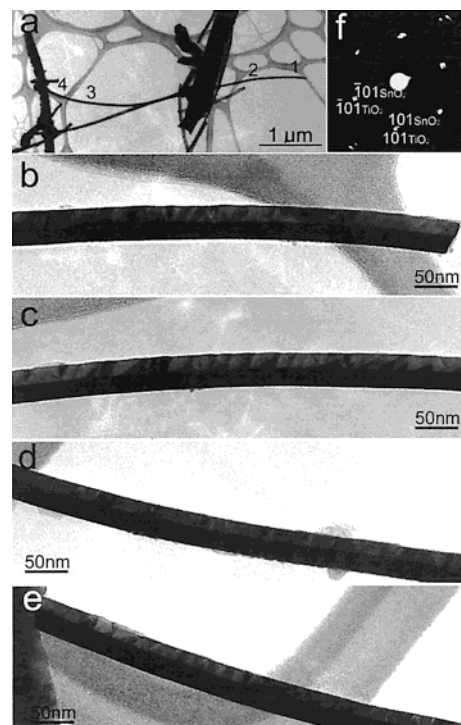

Figure 4. TEM images of a ~5 μm long $Co_{0.05}Ti_{0.95}O_2$@SnO_2 nanotape produced by PLD. Images (b−e) were taken on this individual nanotape as shown in (a), areas (1−4), respectively. (f) Electron diffraction pattern recorded at the interface. These structures were synthesized by ablating a $Co_{0.05}Ti_{0.95}O_2$ target at 700 °C in 125 mTorr of O_2 using laser ablation parameters similar to those described in Figure 1.
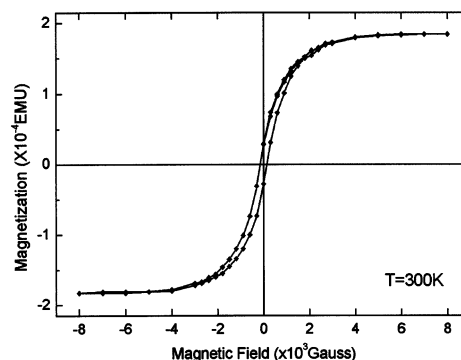

Figure 5. An M−H curve for a $Co_{0.05}Ti_{0.95}O_2$@SnO_2 nanotape sample taken at room temperature. The data were recorded using a superconducting quantum interference device magnetometer (Quantum Design MPMS).

The methodology reported here is highly versatile, and we focus on the TiO_2@SnO_2 nanotape system only as a showcase introduction to this powerful synthetic approach. It should be possible to fabricate highly crystalline nanotapes or core−sheath structures of many other complex materials using different metal oxide nanoribbons (ZnO, MgO, Al_2O_3)[9,14,15] as substrates. Important features of this nanoribbon-based approach to lateral heterostructure formation reside in its flexibility in materials choice, synthetic simplicity, and high-quality epitaxial structures, which differ significantly from previously reported core−sheath structures.[16,17] Possible nanotape functionalities are essentially unlimited, and could readily include luminescent, ferro-

magnetic (transition metal doped TiO_2 and ZnO, $LaMnO_3$), ferroelectric ($BaTiO_3$, $PbTiO_3$), and superconducting ($YBa_2Cu_3O_z$) properties. These composite bimorph nanotapes represent a novel class of highly functional, one-dimensional nanoscale building blocks for nanowire-based devices.

References

(1) Yang, P.; Wu, Y.; Fan, R. *Inter. J. Nano.* **2002**, *1*, 1−39.
(2) Huang, M. et al. *Science* **2001**, *292*, 1897−1899.
(3) Hu, J.; Odom, T. W.; Lieber, C. M. *Acc. Chem. Res.* **1999**, *32*, 435−441.
(4) Wu, Y.; Fan, R.; Yang, P. *Nano Lett.* **2002**, *2*, 83−87.
(5) Björk M. T. et al. *Nano Lett.* **2002**, *2*, 88−89.
(6) Gudiksen, M. S.; Lauhon, L. J.; Wang, J.; Smith, D. C.; Lieber, C. M. *Nature* **2002**, *415*, 617−620.
(7) Kwan, S.; Kim, F.; Arkana, J.; Yang, P. *Chem. Commun.* **2001**, *5*, 447−448.
(8) Urban, J. J.; Yun, W. S.; Gu, Q.; Park, H. *J. Am. Chem. Soc.* **2002**, *124*, 1186−1187.
(9) Pan, Z. W.; Dai, Z. R.; Wang, Z. L. *Science* **2001**, *291*, 1947−1949.
(10) Chambers S. A. et al. *Appl. Phys. Lett.* **2001**, *79*, 3467−3469.
(11) Matsumoto, Y. et al. *Jpn. J. Appl. Phys.* **2002**, *40*, L1204−1206.
(12) Park, W. K.; et al. *J. Appl. Phys.* **2002**, *91*, 8093−8095.
(13) Matsumoto, Y. et al. *Science* **2001**, *291*, 854−856.
(14) Yang, P.; Lieber, C. M. *Science* **1996**, *273*, 1836−1840.
(15) Huang, M. H.; Wu, Y.; Feick, H.; Weber, E.; Yang, P. *Adv. Mater.* **2001**, *13*, 113−117.
(16) Wang, Z. L. et al. *Appl. Phys. Lett.* **2000**, *77*, 3349−3351.
(17) Zhang, Y.; Suenaga, K.; Colliex, C.; Iijima, S. *Science* **1998**, *281*, 973−975.

NL0257216